

Article

# A Novel Physics-Informed Hybrid Modeling Method for Dynamic Vibration Response Simulation of Rotor–Bearing System

Mengting Zhu, Cong Peng <sup>\*</sup>, Bingyun Yang and Yu Wang

College of Automation Engineering, Nanjing University of Aeronautics and Astronautics, Nanjing 211106, China; peanutzmt@nuaa.edu.cn (M.Z.); yby@nuaa.edu.cn (B.Y.); yu\_wang\_1019@nuaa.edu.cn (Y.W.)

\* Correspondence: pengcong@nuaa.edu.cn

**Abstract:** For rotor–bearing systems, their dynamic vibration models must be built to simulate the vibration responses that affect the safe and reliable operation of rotating machinery under different operating conditions. Single physics-based modeling methods can be used to produce sufficient but inaccurate vibration samples at the cost of computational complexity. Moreover, single data-driven modeling methods may be more accurate, employing larger numbers of measured samples and reducing computational complexity, but these methods are affected by the insufficient and imbalanced samples in engineering applications. This paper proposes a physics-informed hybrid modeling method for simulating the dynamic responses of rotor–bearing systems to vibration under different rotor speeds and bearing health statuses. Firstly, a three-dimensional model of a rolling bearing and its supporting force are introduced, and a physics-based dynamic vibration model that couples flexible rotors and rigid bearings is constructed using multibody dynamics simulation. Secondly, combining the simulation vibration data obtained using the physics-based model with measured vibration data, algorithms are designed to learn vibration generation and data mapping networks in series connection to form a physics-informed hybrid model, which can quickly and accurately output the vibration responses of a rotor–bearing system. Finally, a case study on the single-span rotor platform is provided. By comparing the signal output by the proposed physics-informed hybrid modeling method with the measured signal in the time and frequency domains, the effectiveness of proposed method under both constant- and variable-speed operating conditions are illustrated.

**Keywords:** dynamic vibration response; physics-informed; modeling; rotor–bearing system



**Citation:** Zhu, M.; Peng, C.; Yang, B.; Wang, Y. A Novel Physics-Informed Hybrid Modeling Method for Dynamic Vibration Response Simulation of Rotor–Bearing System.

*Actuators* **2023**, *12*, 460. <https://doi.org/10.3390/act12120460>

Academic Editors: Zongli Lin and Young-Tai Choi

Received: 7 November 2023

Revised: 2 December 2023

Accepted: 8 December 2023

Published: 11 December 2023



**Copyright:** © 2023 by the authors. Licensee MDPI, Basel, Switzerland. This article is an open access article distributed under the terms and conditions of the Creative Commons Attribution (CC BY) license (<https://creativecommons.org/licenses/by/4.0/>).

## 1. Introduction

The rotor–bearing system plays a crucial role in rotating machinery, and its behavior directly affects the safety and stability of machinery operation. Rolling bearings are important supporting components used to transmit motion and carry load. They are widely adopted in high-precision and high-speed rotating machinery, such as motors, aero engines, and wind turbine gearboxes [1,2]. The vibration caused by bearing faults, once it exceeds an allowable level, leads to unexpected failures and shorter lifetime of the bearings [3–5]. Therefore, it is necessary to explore the modeling methods used to simulate the dynamic response of the rotor–bearing systems to vibration for different bearing health statuses and rotor rotational speeds.

In recent years, many scholars have studied physics-based modeling methods of dynamic vibrations for rotor–bearing systems under different operating conditions [6]. Singh et al. [7] reviewed the development of analytical and finite element models for predicting the vibration response of rolling element bearings with localized and extended defects. McFadden et al. [8] established a dynamic vibration model for rolling bearings that considers the vibration caused by the inner-race fault of bearings and modeled vibration as

a pulse sequence with a constant frequency. Ren et al. [9] expanded the dynamic vibration model of rolling bearings to the outer-race and rolling element fault conditions, and they studied the influences of load distribution and fault location on the dynamic vibration characteristics. Liu et al. [10] constructed a dynamic model with 12 degrees of freedom for a rigid rotor–bearing system. This model includes a half-sinusoidal function to represent the additional excitation caused by bearing faults, and the influence of coupling between rigid rotor and bearing is taken into account. Wang et al. [11] introduced a nonlinear bearing model and established a dynamic model of a dual-rotor system based on the finite element method. Li et al. [12] and Brouwer et al. [13] used the finite element method to build a dynamic vibration model for a flexible rotor–bearing system. The two models integrate the rigid motion and elastic vibration of a rotor and revealed that the flexible deformation of a rotor affects the bearing displacement and orientation. Wang et al. [14] used the multibody dynamic simulation method to establish a dynamic three-dimensional vibration model for rotor–bearing systems, which can be used to simulate the actual bearing fault pattern by changing the geometric model. Liu et al. [15] discussed the influence of the relative motion of a bearing caused by the cage clearance on the lubrication characteristics of the local contact area. This also inevitably affects the calculation of contact and friction and introduces flexible vibrations into the bearing force. These above models reflect the impact of bearing faults on the dynamic vibration response and generate a large and diverse amount of simulated vibration data. However, due to the numerous vibration sources in complex rotor–bearing systems, the vibration signals simulated using physics-based models often differ from actual measured signals.

Data-driven dynamic vibration modeling methods are used to analyze the intrinsic relationship between dynamic vibration responses and operating conditions via mining the actual measured vibration data [16]. Popescu et al. [17] presented a novel method for the detection and optimal segmentation of changes in vibrating signals to investigate the points of vibration response change generated by the faults. Yan et al. [18] proposed a health index to describe machine faults and explored the relationship between the health index and fused vibration spectrum amplitudes. Wang et al. [19] proposed a multi-input and multitask convolutional neural network to construct a numerical model that autonomously learn fault characteristics from vibration signals in the time, frequency, and time–frequency domains. This model describes the dynamic vibration responses for different defect locations and rolling bearing sizes. Wang et al. [20] developed a coupled hidden Markov fusion method that integrates the fault characteristics extracted from multichannel measured vibration signals, which better fit the analytical relationship between dynamic vibration responses and bearing faults. Shao et al. [21] built an auxiliary classifier generative adversarial network (GAN) for modeling the signal generation process, and they generated synthetic vibration signals with bearing fault labels. Zhang et al. [22] proposed a Wasserstein GAN based on the quality assessment of samples. The Wasserstein distance allows the discriminator to provide more meaningful gradient information to the generator and improves the consistency of the generated vibration samples with the actual measured samples. Liu et al. [23] proposed a deep feature enhanced GAN, and the self-attention module in this network was designed to enhance the feature extraction ability, which improved the accuracy and diversity of the generated vibration samples under different bearing faults. The above models, driven by measured vibration signals, more closely mimic actual rotor–bearing systems, but their modeling accuracy depends heavily on the number and distribution of the measured samples. In the absence of a sufficient number of measured samples, the generated vibration signal is inconsistent with the measured signals.

To resolve the above problems, the combination of physics-based and data-driven modeling methods is regarded as effective; examples of these methods include physical-informed neural networks [24] and digital twins [25]. Li et al. [26] integrated physical information into a neural network to construct the network structure of Reynolds-equation-controlled flow neural networks. With a physical-informed neural network, the aerodynamic characteristics of gas bearing were then predicted. Thelen et al. [27] pointed out

that digital twins integrate the best available physical models, sensor updates, and history data to mirror the life of a physical entity. In [28], the adopted artificial intelligence model invokes a numerical model and sensor data as the input to predict the structural performance of key components of heavy equipment. Piltan et al. [29] proposed an adaptive algorithm for fault diagnosis and crack size identification in bearings. The mathematical model of dynamic vibrations under normal operating conditions was firstly built with the Gaussian process regression method, and vibration responses for different types and sizes of bearing faults were then estimated using the designed residual signal observer. Qin et al. [30] proposed a data model combined with a digital twin of the life cycle of a rolling bearing. The predicted evolution of bearing defectd was introduced into a mathematical dynamic model of a bearing, and CycleGAN, driven by the measured life-cycle data, was designed to correct the vibration responses of the mathematical dynamic model. Wang et al. [31] established a dynamic model of a rotor system used for unbalanced quantification and localization. The dynamic vibration model with rotor imbalances was built using multiphysics simulation; a model update strategy, with measured critical speed and vibration amplitude as the updated references, was used to optimize the dynamic model. However, the above methods mostly focus solely on the rotor or bearing components in physics-based modeling, and the rotor–bearing coupling and the operating condition of variable speeds on dynamic vibrations have not been taken into account. Moreover, the number of vibration samples is often insufficient, despite this situation being common during the actual operation of rotating machinery under a wide speed range; however, the above methods pay little attention to dynamic vibration modeling in this scenario.

This study developed a physics-informed hybrid modeling method for a dual-disc rotor–bearing system for typical bearing health statuses to simulate its dynamic responses to vibration at different speeds. Considering the geometric morphology of rolling bearings and the structural characteristics of flexible rotors, a physics-based dynamic vibration model was firstly constructed with the support of dynamics mechanism and professional multibody simulation software. To improve the efficiency of the physics-based model, the simulated vibration dataset was then established, and the vibration generation network was trained to quickly generate vibration signals at different speeds and typical bearing health statuses. After that, the data mapping network was designed to map the generated vibration samples onto their measured vibration sample counterparts. With the combination of the two networks, the physics-informed hybrid model of dynamic vibrations was formed, which is expected to output simulated dynamic vibration responses that approximate the measured ones.

In remainder of this article, Section 2 describes the vibration mechanism of a rotor–bearing system and introduces the implementation of the numerical simulation using the physics-based dynamic vibration model. Section 3 describes the physics-informed hybrid modeling method based on the combination of a simulated vibration dataset, a measured vibration dataset, and the learning algorithms of the vibration generation network and data mapping network. Section 4 takes a single-span rotor platform as example and illustrates this specific implementation and experimental results. Section 5 concludes this paper.

## 2. Physics-Based Dynamic Vibration Model of Rotor–Bearing System

### 2.1. Preliminary

Figure 1 shows a schematic diagram of a dual-disc rotor–bearing system. As shown in Figure 1, two discs are fixed on the rotor, and both ends of rotor are supported by rolling bearings.  $O_2$  and  $O_3$  are the centroids of two discs.  $O_1$ , and  $O_4$  are the geometric centers of two rolling bearings.  $x_i$  and  $y_i$  are displacements, respectively, in the  $x$ -axis and  $y$ -axis directions at  $O_i$ , where  $i = 1, 2, 3, 4$ .

According to Newton’s second law and the Lagrange equation, the differential equation of the motion of a rotor–bearing system is represented as,

$$\begin{cases} m_1 \ddot{x}_1 + c_{s1} \dot{x}_1 + k_1(x_1 - x_2) = F_{ax} \\ m_1 \ddot{y}_1 + c_{s1} \dot{y}_1 + k_1(y_1 - y_2) = F_{ay} - m_1 g \\ m_2 \ddot{x}_2 + c_{d1} \dot{x}_2 + k_2(x_2 - x_1) + k_2(x_2 - x_3) = 0 \\ m_2 \ddot{y}_2 + c_{d1} \dot{y}_2 + k_2(y_2 - y_1) + k_2(y_2 - y_3) = -m_2 g \\ m_3 \ddot{x}_3 + c_{d2} \dot{x}_3 + k_3(x_3 - x_2) + k_3(x_3 - x_4) = 0 \\ m_3 \ddot{y}_3 + c_{d2} \dot{y}_3 + k_3(y_3 - y_2) + k_3(y_3 - y_4) = -m_3 g \\ m_4 \ddot{x}_4 + c_{s2} \dot{x}_4 + k_4(x_4 - x_3) = F_{bx} \\ m_4 \ddot{y}_4 + c_{s2} \dot{y}_4 + k_4(y_4 - y_3) = F_{by} - m_4 g \end{cases} \quad (1)$$

where  $m_1$  and  $m_4$  are the equivalent masses of the rotor at  $O_1$  and  $O_4$ .  $m_2$  and  $m_3$  are the masses of the discs.  $c_{s1}$  and  $c_{s2}$  are the damping of the rotor at  $O_1$  and  $O_4$ .  $c_{d1}$  and  $c_{d2}$  are the damping of the rotor at  $O_2$  and  $O_3$ .  $k_1, k_2, k_3, k_4$  indicate the stiffness of the rotor at  $O_i$ .  $g$  is the acceleration due to gravity.

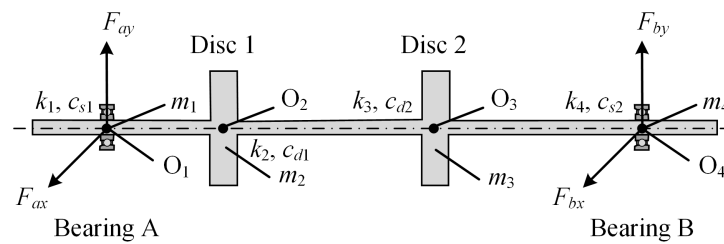


Figure 1. Schematic diagram of dual-disc rotor–bearing system.

It can be observed from (1) that the dynamic characteristics of a rotor–bearing system are not only affected by rotor speed but also by the supporting force of the bearing. According to Hertzian contact theory, the nonlinear supporting forces  $F_{bx}$  and  $F_{by}$  of a rolling bearing in the  $x$  and  $y$  directions are the sum of the contact forces between rolling elements and races. The supporting forces are represented as

$$\begin{cases} F_{bx}(x, y, \omega, t) = k_b \sum_{j=1}^{N_b} \delta_j^{3/2} \sin \theta_j \\ F_{by}(x, y, \omega, t) = k_b \sum_{j=1}^{N_b} \delta_j^{3/2} \cos \theta_j \end{cases} \quad (2)$$

where  $k_b$  is the Hertz elastic coefficient.  $j$  is the index of rolling elements, where  $j = 1, 2, \dots, N_b$ .  $N_b$  is the number of rolling elements.  $\theta_j$  denotes the rotating angle at time  $t$  of the  $j$ th rolling element.

When the health status of a bearing is normal, the contact deformation  $\delta_j$  of the  $j$ th rolling element is represented as

$$\delta_j = (x_{in} - x_{out}) \cos \theta_j + (y_{in} - y_{out}) \sin \theta_j - \mu \quad (3)$$

where  $\mu$  is the initial radial clearance of the rolling bearing.  $(x_{in}, y_{in})$  are the displacements of the inner race, and  $(x_{out}, y_{out})$  are the displacements of the outer race.

When the health status of a bearing is defected, an additional displacement excitation  $\delta_d$  is injected. As the rolling element passes through the defected area, periodic vibration occurs in the supporting force of the bearing. The contact deformation  $\delta_j$  of the  $j$ th rolling element is expanded as

$$\delta_j = (x_{in} - x_{out}) \cos \theta_j + (y_{in} - y_{out}) \sin \theta_j - \mu - \beta \delta_d \quad (4)$$

where  $\beta$  is the switching variable indicating the health status of the bearing. In bearing damage scenarios, the manifestations typically include cracks, spalling, and pitting, with these forms of damage often presenting in irregular shapes. In this paper, the outer-race

bearing fault is discussed as a representative defect, and the shape of defect area is assumed to be a square. This assumption is predicated on the fact that a square shape provides distinct boundary conditions, thereby facilitating a more detailed analysis of the impact of the status of bearing health on the vibration characteristics of a rotor system. Thus, the bearing's health state includes normal bearings and defected bearings, which correspond to two values of variable  $\beta$ . To be specific, normal refers to a healthy bearing, and defect refers to a bearing that contains a defected area of defined length, width, and depth.

When the rolling element is located within the angular span of the defect area, there is deformation release. The displacement excitation caused by an outer-race fault of a bearing can be represented as [10]

$$\delta_d = \begin{cases} \delta_{d\max} \cos\left(\frac{(\theta_j - \varphi_0)\pi}{2\varphi_d}\right), & \varphi_0 - \varphi_d < \theta_j \leq \varphi_0 + \varphi_d \\ 0, & \text{otherwise} \end{cases} \quad (5)$$

where  $\varphi_0$  is the initial angular of the defect area, and  $\varphi_d$  is the angular span of the defect area.  $\delta_{d\max}$  denotes the maximum value of the displacement excitation and is represented as

$$\delta_{d\max} = r - \sqrt{(r)^2 - (L/2)^2} \quad (6)$$

where  $r$  is the radius of the rolling element, and  $L$  is the length of the defect area.

It can be observed from the above analysis that the dynamic vibration model of a rotor–bearing system is affected by the rotating speed of the rotor, health status of the bearing, and size of the defect area.

## 2.2. Numerical Simulation Implementation Using Physics-Based Model

To implement the physics-based dynamic vibration modeling for a rotor–bearing system, ADAMS (Automatic Dynamic Analysis of Mechanical System) software was adopted for numerical simulations. This numerical simulation focused on the vibration acceleration responses under different rotating speeds of the rotor and health statuses of the bearing. Its implementation included the following procedures

*Procedure 1:* Modeling of multibody rotor–bearing system.

Firstly, the overall geometric model of the rotor–bearing system was drawn in SolidWorks and imported into ADAMS. As shown in Figure 2, the geometric model included the rotor, discs, cage, outer race, inner race, rolling elements, bearing pedestals, and base. Secondly, by adding material parameters to these geometric bodies and substituting the rotor and two bearing pedestals with flexible bodies, physical properties such as mass, centroid position, stiffness, and moment of inertia were provided to the geometric model.

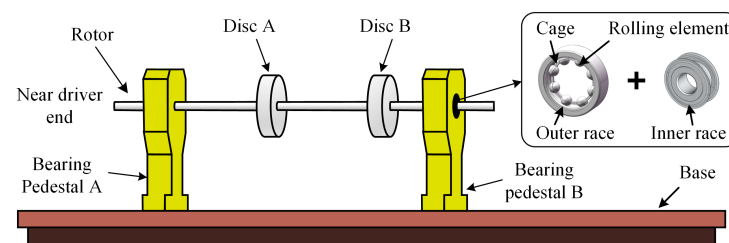


**Figure 2.** The overall geometric model of a rotor–bearing system.

Figure 3 presents the finite element models of the flexible rotor and bearing pedestals, which are connected to other rigid bodies through rigid nodes. The flexibility of the rotor was considered in the inherent structural and material characteristics of the rotor itself, which result in vibrations during its operation. Given the complexity of rigid–flexible coupling modeling and in the interest of enhancing simulation efficiency, a free meshing method was selected in ANSYS APDL for the rotor's solid meshing, with the smart mesh sizing level set to 3. Key points were created at the center of the bearing locations on both

sides of the rotor mesh model, leading to the generation of nodes 40490 and 40491, as shown in Figure 3a. Utilizing these key points as primary nodes and the surrounding nodes as secondary nodes, a spider-web-like rigid region was established. This configuration ensured that the forces applied through the primary node were distributed across various secondary nodes on the rotor's cross-section. As shown in Figure 3a, the flexible model of the rotor primarily employed triangular elements to accommodate regions with deformation or highly nonlinear behavior. On both sides of the rotor, quadrilateral elements were automatically selected. This choice was motivated by the enhanced precision offered by quadrilateral elements when applying boundary conditions at the two nodes. Their size compared to the diameter of the shaft was about one-quarter of the scale. Similarly, the free meshing approach with the smart mesh sizing level set to 3 was employed for the mesh division of the bearing pedestal model, as shown in Figure 3b. This division was predicated on the ability to obtain nodes corresponding to the positions where accelerometer sensors were mounted on the experimental platform, thereby facilitating the measurement of the vibration response at these specific nodes.

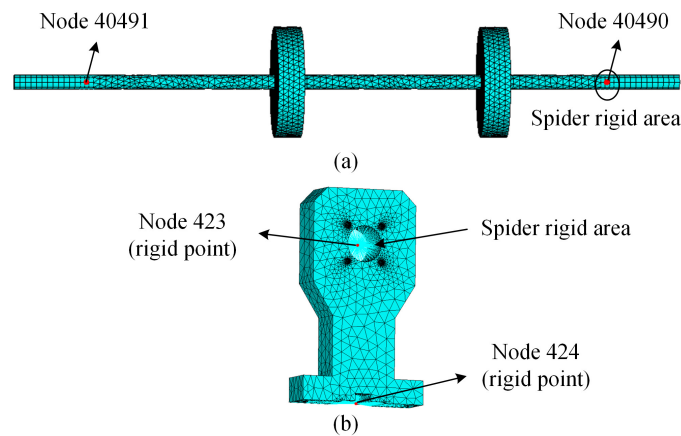


**Figure 3.** Finite element models of flexible bodies. (a) Rotor, (b) bearing pedestal.

Thirdly, connections between different geometric bodies are defined, as shown in Table 1, and employed to constrain the motion of the rotor–bearing system. The stiffness and damping parameters of the spring–damping constraint between the bearing pedestal and the base were set to  $15.1 \times 10^6$  N/m and 2210.7 Ns/m according to [14]. Finally, the numerical simulation for dynamics of the rotor–bearing system was driven by adding a motion that rotated around the  $z$ -axis at the end of the rotor. The WSTIFF integration method is an implicit numerical integration algorithm with the ability to adaptively adjust step size and order for numerical simulation solutions, which exhibits high numerical stability in long-term simulations. Meanwhile, considering the high computational complexity caused by rigid–flexible coupling and the contact constraints in numerical simulation model, the I3 integrator form was employed. Thereupon, the vibration acceleration response  $F_{acc}(\omega, x_0, y_0, z_0, t)$  of arbitrary coordinates  $(x_0, y_0, z_0)$  at different rotating speeds  $\omega$  of rotor was solved using the WSTIFF I3 integrator.

**Table 1.** Connections between geometric bodies of rotor–bearing system.

1st Body	2nd Body	Constraint Type
Base	Ground	Fixed joint
Bearing pedestal	Base	Spring-damping
Outer race	Bearing pedestal	Fixed joint
Inner race	Rotor	Fixed joint
Rolling element	Outer race, inner race	Contact force
Rolling element	Cage	Spherical joint

*Procedure 2: Modeling of bearing supporting force.*

According to (1), the supporting force of a bearing is one of the critical factors affecting the dynamic responses of rotor–bearing systems. In a previous work [31], a spring–damper was often used in the numerical simulation to simplify the actual support of a rolling bearing. The simplified supporting force generated by the spring–damper can be expressed as

$$F_{bx} = -k_{eq}(u - u_0) - c_{eq}\dot{u} + F_{preload} \quad (7)$$

where  $k_{eq}$  is the stiffness coefficient of the rolling bearing, and  $c_{eq}$  is the damping coefficient.  $u$  is the length of the spring.  $F_{preload}$  is the preload of the spring, and  $u_0$  is the displacement caused by the preload.

According to (2), the supporting force of a rolling bearing is essentially related to the contact force of each rolling element. Nevertheless, the spring–damper expressed in (7) struggles to describe the interaction between rolling elements and raceways and especially the influence of raceway defects on the dynamic responses of rotor–bearing systems. Here, the contact constraints between the rolling element, inner-race raceway, and outer-race raceway, as well as the geometric model of the rolling bearing, were introduced to improve the dynamic vibration model of rotor–bearing systems. The contact between the rolling element and raceway was regarded as a solid-to-solid type, and the impact function method was adopted to calculate the contact force. In the ADAMS environment, the normal contact force between each rolling element and raceway is represented as [32]

$$F_j = \begin{cases} K(r - x_j)^\zeta - c_{max}\dot{x}_j \times STEP(x_j, r - d, C, r, 0), & \text{if } x_j > r \\ 0, & \text{if } x_j \leq r \end{cases} \quad (8)$$

where  $d$  is the penetration depth, and its value was set to  $1 \times 10^{-5}$  m.  $\zeta$  is the force exponent; from experience, it can be said that hard metals require a value of 2.2.  $K$  is the equivalent contact stiffness, and  $C$  is the equivalent contact damping, which were evaluated with Hertzian contact theory. Here, the contact stiffness and damping were set to  $1 \times 10^{11}$  N/m and 20 Ns/m according to reference [14].  $x_j$  is the distance from the geometry center of the  $j$ th rolling element to the raceway.

For the friction force, the Coulomb friction model was adopted, which was calculated through multiplying the coefficient of friction  $\mu_0$  for every slip velocity  $v_s$  by the normal force [14]. The coefficient of friction can be represented as

$$\mu_0 = \begin{cases} \mu_s \times STEP(abs(v_s), -V_s, -1, V_s, 1) \times sgn(v_s), & \text{if } abs(v_s) < V_s \\ STEP(abs(v_s), V_s, \mu_s, V_d, \mu_d) \times sgn(v_s), & \text{if } V_s < abs(v_s) < V_d \\ \mu_d \times sgn(v_s), & \text{if } abs(v_s) > V_d \end{cases} \quad (9)$$

where  $\mu_s$  and  $\mu_d$  are the static and dynamic coefficients of friction, which can be found for different contact materials in reference [33].  $V_s$  and  $V_d$  are the static and dynamic transition velocities, which can be designated according to experience. The four parameters here were set to  $\mu_s = 0.8$ ,  $\mu_d = 0.76$ ,  $V_s = 1 \times 10^{-4}$  m/s, and  $V_d = 1 \times 10^{-2}$  m/s.

*Procedure 3: Modeling of outer-race bearing fault.*

Benefiting from the introduction of a geometric bearing model, outer-race faults can be modeled by selecting different shapes of slots and sections on the geometry model. Figure 4 shows geometric bearing models without and with outer-race faults. Through replacing the normal bearing at the far end of the motor driver with a bearing with an outer-race fault, the dynamic vibration model of a rotor–bearing system with a bearing fault was further established. Here, the bearing health status is embedded as an additional variable  $\beta$  to expand the dynamic vibration model, and the vibration acceleration response  $F_{acc}(\omega, \beta, x_0, y_0, z_0, t)$  at different rotor speeds and bearing health statuses can be obtained via numerical simulation.

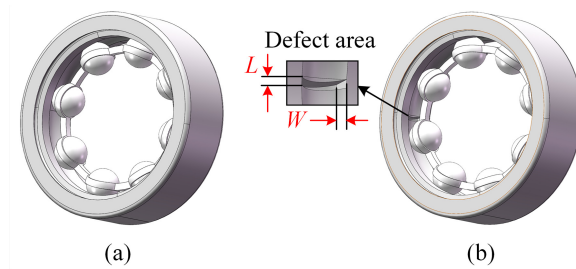


**Figure 4.** Geometric models of bearing. (a) Normal bearing without fault, (b) defected bearing with outer-race fault.

### 3. Physics-Informed Hybrid Modeling Method

In this section, a physics-informed hybrid modeling method, as sketched in Figure 5, is proposed. With the simulated vibration responses obtained using the physics-based dynamic model, the vibration generation network was designed to quickly generate vibration signals under different operating conditions, including different rotor speeds, and bearing health statuses. To improve the accuracy of the dynamic vibration model, which was combined with measured vibration signals, a data mapping network was designed to correct the generated vibration signals into corresponding signals that approximate the measured ones. In this way, through combination with the physics-based model, algorithms of vibration generation and data mapping, and measured vibration data, a physics-data hybrid model was established, as shown in Figure 5a.

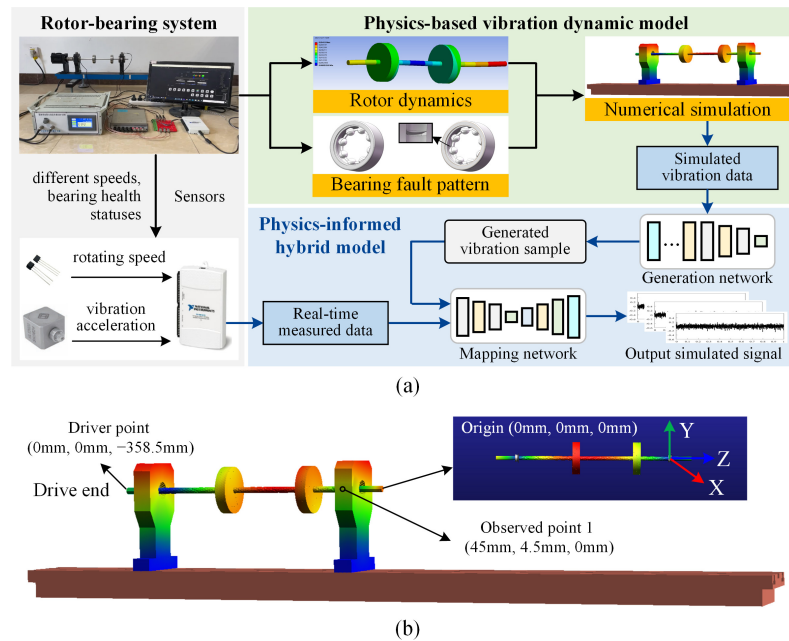


**Figure 5.** The proposed physics-informed hybrid modeling method. (a) Overall architecture, (b) diagram of Cartesian coordinate system involved in ADAMS.

#### 3.1. Description of Simulated and Measured Vibration Datasets

Samples of the simulated vibration dataset were observed from the physics-based numerical simulation model, and samples of the measured vibration dataset were collected from an actual rotor–bearing test rig. The simulated and measured vibration datasets included radial horizontal vibration signals collected at different rotor speeds and bearing health statuses, which were observed on the bearing pedestal away from the motor driver. They both contained 22 sets of operating conditions for 11 types of rotor speeds and 2 types of bearing statuses. The specific numerical simulation parameters of the physics-based model are listed in Table 2.

**Table 2.** Numerical simulation parameters of physics-based model.

Parameter Type	Parameter	Value
Operating conditions	Rotor angular speed ( $\omega$ /rpm)	1000–2000
	Bearing health status ( $\beta$ )	0, 1
Process-dependent parameters	Width of defect area ( $W$ /mm)	1
	Length of defect area ( $L$ /mm)	0.5
	Observed Cartesian generalized coordinates (mm)	(45, 4.5, 0)
Simulation parameters	Length per sample (s)	1
	Step size per sample	1/2000

To obtain the simulated vibration samples, these steps were followed: Firstly, the original health status of the bearing was defined as normal, where  $\beta$  was set to 0. When the health status of the bearing was switched to 1, the geometric model of the normal bearing was substituted with a defected bearing with an outer-race fault. The length of the defect area in the outer race was 0.5 mm, and the width was 1 mm. Secondly, a motion around the z-axis was applied to drive the rotor to rotate. The speed of motion ranged from 1000 rpm to 2000 rpm, and numerical simulations were repeated in 100 rpm intervals. At the same time, the simulated vibration acceleration signals were observed and recorded. As illustrated in Figure 5b, the Cartesian coordinate system was defined in ADAMS, with node 40490 of the rotor's flexible model serving as the origin, which was assigned coordinates of (0 mm, 0 mm, 0 mm). This node coincided with the center point of the inner race of the bearing as well as the flexible model node 423 of the bearing pedestal. The observation point was located at the center of the side surface of the bearing pedestal at the nondriving end of the rotor, with the corresponding coordinates being (45 mm, 4.5 mm, 0 mm). It corresponded to the right point of the bearing pedestal away from the motor driver. The coordinate for the point of motor drive application on the rotor was (0 mm, 0 mm, −358.5 mm). The length of each vibration sample was 1 s, and the step size was set to 1/2000. And these observed vibration samples made up the simulated vibration dataset.

### 3.2. Construction of Vibration Generation Network

Figure 6 presents a flow chart of the physics-informed hybrid modeling method based on vibration generation and data mapping networks. With the simulated vibration dataset, the vibration generation network  $G$  was designed to convert the physics-based numerical simulation model of dynamic vibration into a reduced numerical model. This network takes the operating condition vectors  $\{v_n\}_{n=1}^{N_v}$  ( $v_n \in \mathbf{V}$ ) as the input, and takes the vibration signals  $\{s_n\}_{n=1}^{N_s}$  ( $s_n \in \mathbf{X}$ ) simulated via numerical simulation as the truth. The basic structure of this network adopts a fully connected network and is described as

$$\tilde{s}_n = G(v_n(\omega, \beta)) \quad (10)$$

where  $\tilde{s}_n$  denotes the signal generated by the trained vibration generation network.

A structure diagram of the vibration generation network is shown in Figure 7a, and the specific network parameters are listed in Table 3. It is noted that the first three linear layers utilize the leaky ReLU nonlinear activation function, and the network adopts the He initialization method. This initialization method does not drastically change the strength of the input signal, which allows the network to capture more useful data features.

**Table 3.** Structure parameters of the vibration generation network.

Network Layer	Output Size	Operator
Linear1	11 × 1 × 128	Leaky_ReLU
Linear2	11 × 1 × 256	Leaky_ReLU
Linear3	11 × 1 × 512	Leaky_ReLU
Linear4	11 × 1 × 1000	Tanh

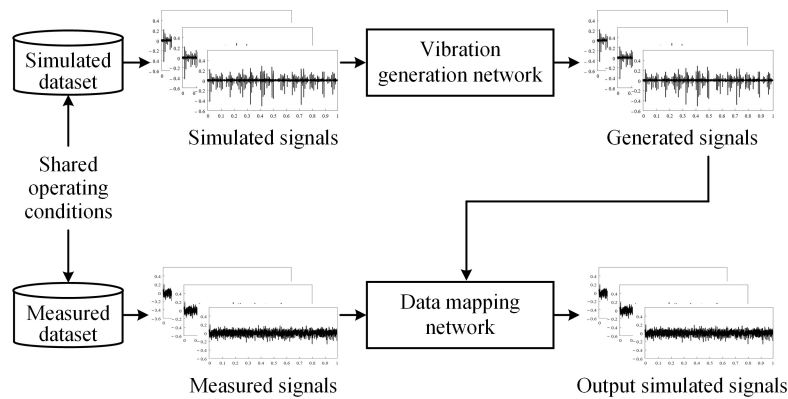


**Figure 6.** Flow chart of hybrid modeling method based on vibration generation and data mapping networks.

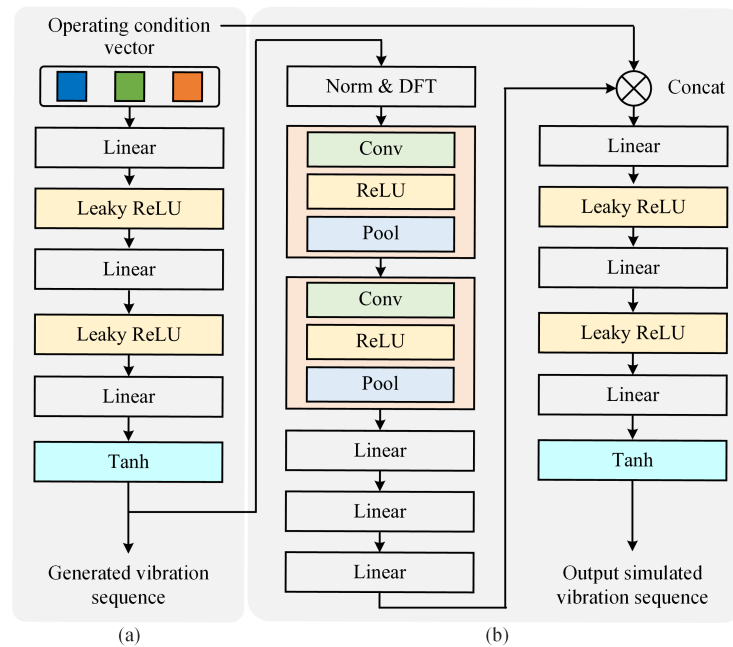


**Figure 7.** The structure diagram of two networks. (a) The vibration generation network, (b) the data mapping network.

Considering the periodic characteristic of vibration signals, the loss function  $L_G$  of the generation network adds a constraint on the basis of the traditional mean squared error (MSE). The improved loss function  $L_G$  was designed to constrain both the frequency and phase of the vibration signals and to achieve better performance for sequence generation tasks. The improved loss function  $L_G$  is represented as

$$L_G = \lambda_1 \frac{1}{N} \sum_{p=1}^{p=N} (\tilde{s}_p - s_p)^2 + \lambda_2 \frac{2}{N} \sum_{p=1}^{p=N/2} (T(\tilde{s}_p) - T(\tilde{s}_p))^2 \quad (11)$$

where  $N$  is the number of sampling points.  $p$  is the index of the sampling points, and its value is defined as  $p = 0, 1, \dots, N - 1$ .  $\lambda_1$  and  $\lambda_2$  are optional weight coefficients. In the specific case in our study, the first parameter  $\lambda_1$  was set to 0.25, and the second parameter  $\lambda_2$  was set to 0.75.  $T$  denotes the discrete Fourier transform.

The reduced numerical model trained based on (10) and (11) could generate vibration signals according to the actual working conditions of the rotor–bearing test rig. This provides effective and efficient support for the following data mapping process.

### 3.3. Construction of Data Mapping Network

The data mapping network in Figure 6 was then designed to correct the generated vibration signals obtained using the vibration generation network, making them consistent with the distribution of the measured signals. It is supposed that the simulated samples  $\{s_n\}_{n=1}^{N_s}$  ( $s_n \in \mathbf{X}$ ) and the measured samples  $\{S_n\}_{n=1}^{N_m}$  ( $S_n \in \mathbf{Y}$ ) are subject to different distributions  $p_{data}(s)$  and  $p_{data}(S)$ . An encoder–decoder network is adopted as the basic structure for realizing data mapping. A structure diagram of the mapping network is shown in Figure 7b. Table 4 lists the specific parameters of the network.

**Table 4.** Structure parameters of the encoder–decoder network.

Module	Network Layer	Output Size	Operator
Encoder	Conv1	$11 \times 3 \times 501$	ReLU, MaxPool
	Conv2	$11 \times 6 \times 249$	ReLU, MaxPool
	Linear1	$11 \times 512$	ReLU
	Linear2	$11 \times 256$	ReLU
	Linear3	$11 \times 10$	–
Decoder	Linear4	$11 \times 128$	Leaky_ReLU
	Linear5	$11 \times 256$	Leaky_ReLU
	Linear6	$11 \times 512$	Leaky_ReLU
	Linear7	$11 \times 1000$	Tanh

The mapping function  $M: \mathbf{X} \rightarrow \mathbf{Y}$  is described as

$$\mathbf{Y}_{S \sim p_{data}(S)} \approx M(\mathbf{X}_{s \sim p_{data}(s)}) \quad (12)$$

In (12), the mapping function  $M$  consists of an encoder subnetwork  $E$  and a decoder subnetwork  $D$ . And the process of the mapping network can be expanded as

$$\tilde{S}_n = D(\text{concat}(v_n(\omega, \beta), E(\xi_n))) \quad (13)$$

where  $\tilde{S}_n$  denotes the signal output by the trained data mapping network.

As expressed in (13), the encoder network firstly represents the generated vibration signal as a low-dimensional eigenvector. The operating condition vector is then concatenated to the eigenvector, and the decoder network converts them into corrected simulated vibration signals. The loss function adopted in this data mapping network is consistent with (11). To summarize, the vibration generation network and data mapping network constitute the physics-informed hybrid model, which outputs the corrected simulated vibration responses. Combined with (10) and (13), the constructed hybrid model can output vibration responses corresponding to the given operating conditions.

## 4. Experimental Verification

### 4.1. Experimental Setup

In order to evaluate the effectiveness of the proposed hybrid modeling method, the dual-disc rotor–bearing test rig presented in Figure 8 was adopted for experiments. The Hall sensor built into the motor driver was employed to collect rotor speed signals. A single-axis accelerometer (ULT2019/V), which was installed on the right side of bearing pedestal, was used to collect vibration signals in the radial horizontal direction. The rotor speed signal and vibration acceleration signal were synchronously recorded using an acquisition card (NI USB-6210) at a frequency of 2000 Hz.

Table 5 lists the parameters of the experimental rotor–bearing platform. The equipped rolling bearing was the SKF 6200Z type. The outer-race fault of bearing was preprocessed via the electrical discharge machining. The length of the defect area was 0.5 mm, and the width was 1 mm. The experimental results were as follows.

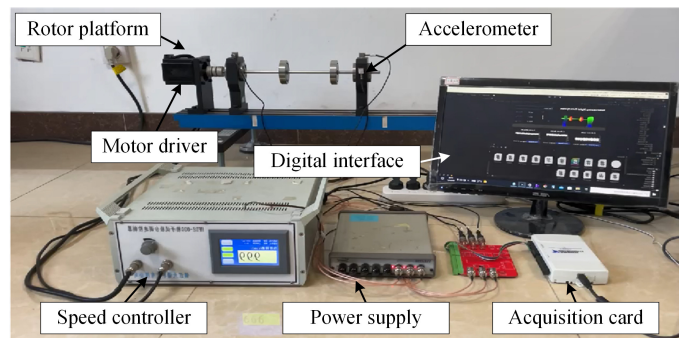


Figure 8. Experimental setup of the dual-disc rotor-bearing platform.

Table 5. Parameters of the experimental rotor-bearing system.

Parameter	Numerical Value
Length of shaft (mm)	460
Radius of shaft (mm)	5
Radius of disc (mm)	38
Thickness of disc (mm)	18
Diameter of rolling element (mm)	4.76
Diameter of inner race (mm)	10
Diameter of outer race (mm)	30
Number of rolling elements	8
Contact angle (°)	49.3

#### 4.2. Numerical Analysis of Physics-Based Dynamic Vibration Model

To evaluate the effectiveness of the numerical simulation in modeling dynamic vibrations, a rotor-bearing system equipped with a normal bearing and equipped with an outer-race bearing fault were separately simulated. Figures 9 and 10 show the simulation results of the rotating speed and vibration acceleration when the rotor was supported by two normal bearings. Theoretically, the rotating speed of the cage can be represented as [32,34]

$$\omega_{cage} = \frac{1}{2}[\omega(1 - \gamma) + \omega_0(1 + \gamma)] \quad (14)$$

where  $\gamma$  is the ratio of the rolling element radius  $r$  to its center-circle radius  $r_c$ .  $\omega_0$  is the rotating speed of the bearing's outer race.

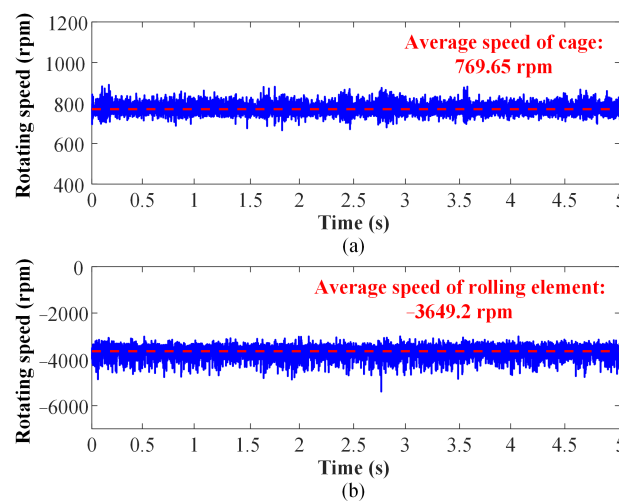
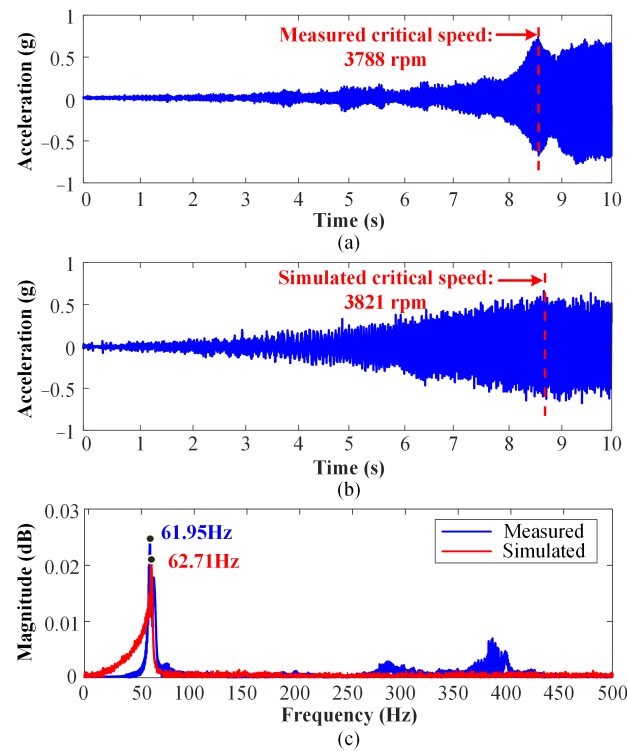


Figure 9. Simulated speed signals of different bearing components when rotor rotates at 2000 rpm. (a) Cage, (b) rolling element.



**Figure 10.** Comparison of vibration signals of a rotor–bearing system under a speed-up condition from 0 rpm to 4000 rpm. (a) The measured signal, (b) the simulated signal, (c) their spectrum results.

The rotating speed of the rolling element can be represented as [32,34]

$$\omega_{roller} = \frac{r_c}{2r}(\omega_0 - \omega)(1 - \gamma)(1 + \gamma) \quad (15)$$

When the rotor operates at a constant speed of 2000 rpm, the theoretical rotating speeds of the cage and rolling element are calculated as 762 rpm and  $-3963.6$  rpm according to (14) and (15). Since the rolling element not only moves with the rotation of the cage but also rotates around itself under the contact of the inner-race and outer-race raceway, its rotational direction is opposite to that of the rotor. Figure 9a presents the simulated rotating speed signal of the cage when the rotor operates at 2000 rpm, and its average speed is 769.65 rpm. Figure 9b presents the simulated speed signal of the rolling element when the rotor operates at 2000 rpm, and its average speed is  $-3649.2$  rpm. Comparing the theoretical and simulated values, the error is less than 7.93%.

When the rotor operates under speed-up conditions, due to the natural frequency characteristics of the rotor, strong vibration occurs at a specific critical speed. The operating condition was set to increase from 0 rpm to 4000 rpm in 10 s for both the experiment and the numerical simulation, and the acceleration process followed the designed S-shaped velocity curve. Figure 10a depicts the measured vibration acceleration signal, which reaches a critical speed of 3788 rpm at 8.58 s. Figure 10b depicts the simulated vibration acceleration signal, which reaches a critical speed of 3821 rpm at 8.72 s. Figure 10c presents their spectrum results, and it can be observed that the frequency component corresponding to the largest vibration amplitude in the measured signal is 61.95 Hz. And, the uppermost frequency component in the simulated signal is 62.71 Hz. The critical speeds and the corresponding frequency components obtained through the numerical simulation and the physical sensor are highly consistent. Therefore, it can be considered that the constraints given in Table 1 and the numerical simulation procedures are feasible.

For a rolling bearing system, a comparison between the numerical simulation and the theoretical model represented in Equations (2)–(6) was conducted. Since the vibration caused by the bearing considered in this study is mainly from a bearing fault, the bearing

system was modeled using the defected bearing with a 1 mm defect width in the outer race. The accuracy of the bearing force was evaluated using the vibration acceleration response, which is proportional to the vibration force and can be easily measured in physical systems. The vibration response calculated using the theoretical model was obtained by solving Equations (2)–(6) using the ode45 algorithm. Similarly, for the numerical simulation model of the bearing system, only the bearing and the bearing pedestal were imported into ADAMS. The contact constraints expressed in Equations (7)–(9), the spring-damping constraint between the bearing pedestal and the ground, and the spherical joint constraint between the cage and rollers were applied according to Table 1. Figure 11 presents a comparison of the vibration signals solved using Equations (2)–(6) and simulated using Equations (7)–(9) at 2000 rpm. It can be observed that both the calculated signal and the simulated signal have 10 shocks within 0.1 s. The corresponding frequency is about 100 Hz. The overall amplitude and curve shape of the calculated signal are basically consistent with those of the simulated signal. Therefore, it is considered reasonable to calculate the bearing force by applying the contact force constraint expressed in Equations (7)–(9) in ADAMS, which can reflect its most obvious vibration characteristics.

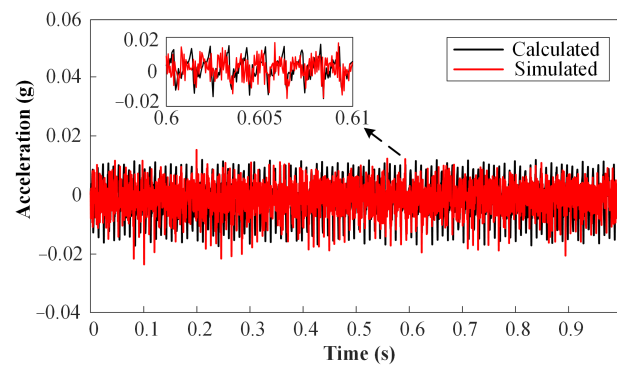


**Figure 11.** Comparison of vibration responses solved using Equations (2)–(6) and simulated by Equations (7)–(9).

For a rotor–bearing system, a further comparison between the numerical simulation and experimental values was conducted. The whole solid model of a rotor–bearing system with a defected bearing was imported into ADAMS for numerical simulation. Figure 12 presents the numerical simulation results of vibration acceleration when the rotor is supported by one normal bearing and one bearing with an outer-race fault at 2000 rpm. According to (4) and (5), the defected bearing with an outer-race fault introduces additional periodic components into the vibration forces. The theoretical characteristic frequency of the fault in the introduced vibration component can be represented as [14]

$$f_{outer} = \frac{N_b}{2}(1 + \gamma)f_\omega \quad (16)$$

where  $f_\omega$  denotes the rotating frequency, which is proportional to the rotating speed of the the rotor.

According to (16), the theoretical characteristic frequency of the bearing outer-race fault is calculated as 101.6 Hz. Figure 12b shows the frequency spectra of the vibration acceleration signals in Figure 12a. In Figure 12b, there are obvious fault characteristic frequencies, with its frequency multiplications in the simulated spectrum, which are 102.8 Hz, 205.6 Hz, 309.6 Hz, and 412.8 Hz, respectively. The error between the obvious fault characteristic frequencies obtained via numerical simulation and their theoretical values is less than 2%. Comparing with the simulated and measured vibration signals, their frequency components are highly consistent. The amplitude at the fault characteristic frequency in the simulated spectrum is  $0.0201 \text{ g}^2/\text{Hz}$ , and the amplitude of the measured spectrum is  $0.0195 \text{ g}^2/\text{Hz}$ , which are also in good agreement. To summarize, the physics-based dynamic

vibration model constructed through numerical simulation is proved to be effective, which can reflect the primary characteristics of a rotor–bearing system.

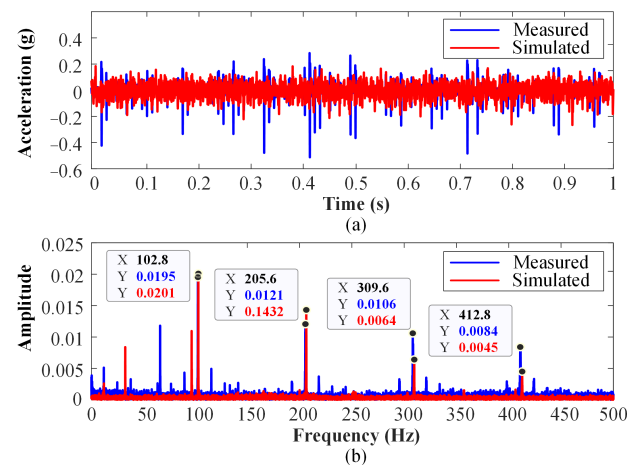


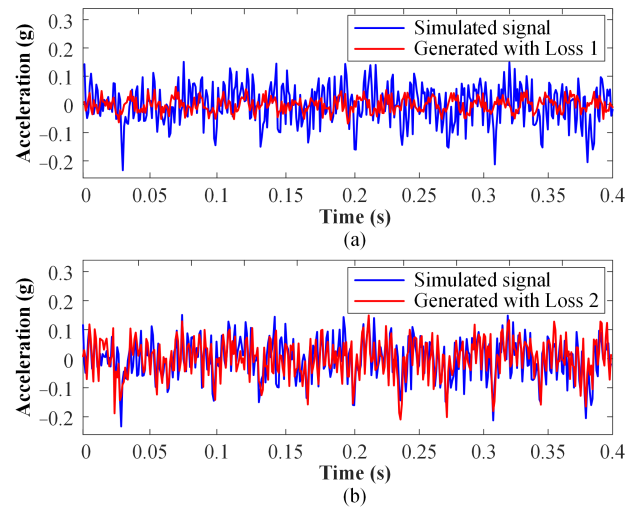
**Figure 12.** Comparison of simulated and measured vibration signals of rotor–bearing system with bearing outer-race fault at 2000 rpm. (a) Acceleration response, (b) frequency spectrum.

#### 4.3. Generation of Simulated Vibration Samples and Their Validation

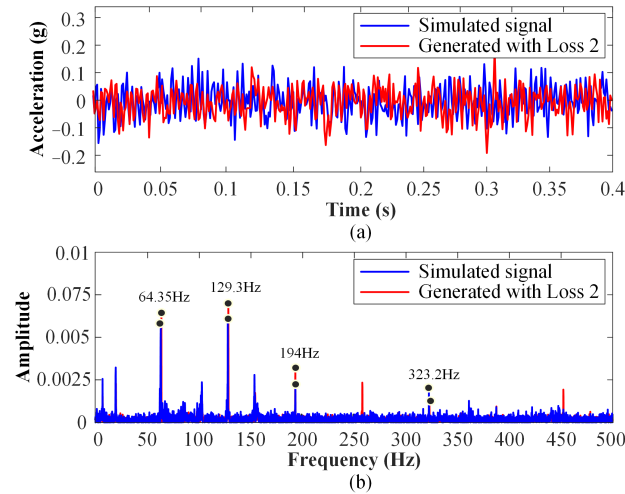
To verify the effectiveness of proposed vibration generation network used to efficiently generate simulated vibration samples under different operating conditions, networks with different loss functions were compared. For the sake of description, the traditional MSE loss function is denoted as Loss 1, and the improved loss function expressed in (11) is denoted as Loss 2. Networks with Loss 1 and Loss 2 were both trained for 300 epochs using the constructed simulated vibration dataset. The feasibility of the vibration generation network was verified by comparing the consistency between the generated signal obtained using the network and the vibration signal obtained from the numerical simulation.

Figure 13 presents the vibration acceleration signals generated using the networks with Loss 1 and Loss 2 when the rotor is supported by one normal bearing and one outer-race fault bearing at a speed of 1200 rpm. It can be observed from Figure 13a that the vibration acceleration response generated using the network with Loss 1 poorly coincides with the numerically simulated response. The MSE value between the two responses is 0.005. In Figure 13b, the vibration signal generated using the network with Loss 2 highly coincides with the numerically simulated response. The MSE value between the two responses is 0.0027. Above results indicate that the proposed loss function can effectively improve the network performance when generating simulated vibration samples. Moreover, the numerical simulation took 36 min and 28 s to generate a 1-second vibration sample, while the trained network took 3.95 s. This proves that the trained vibration generation network can be utilized as an upgraded alternative to numerical simulation and greatly improve the efficiency of generating simulated vibration samples.

For extending the evaluation to test cases outside of the training set points but within the chosen speed range, an additional analysis was conducted. Figure 14 presents a comparison of the signals generated using the vibration generation network with Loss 2 and obtained via simulation at 1250 rpm. It can be seen from Figure 14b that both the generated vibration signal and the simulation one have an obvious outer-race fault characteristic frequency, as well as double, triple, and five times the frequency components; the corresponding amplitude differences are in a relatively small range. This result allows us to demonstrate the network’s generation preference more effectively.



**Figure 13.** Comparison of signals generated using vibration generation network at 1200 rpm. (a) Network with traditional Loss 1, (b) network with improved Loss 2.



**Figure 14.** Comparison of signals generated using vibration generation network with Loss 2 and obtained via simulation at 1250 rpm. (a) Time-domain signals, (b) frequency-domain signals.

#### 4.4. Performance Analysis of Physics-Informed Hybrid Modeling Method

To verify the effectiveness of the proposed hybrid modeling method, the dynamic vibration signals output by the hybrid model were compared with the corresponding measured vibration signals under both constant-speed and variable-speed conditions. And, the WGAN network driven solely using the measured data was adopted as a comparison with the proposed hybrid modeling method. The datasets used for the two conditions are described in Table 6.

**Table 6.** Datasets used for constant-speed and variable-speed conditions.

Operating Condition	Dataset	Rotating Speed (rpm)	Number of Samples
Constant-speed	Simulated dataset	1900	120
	Measured dataset	1900	120
Variable-speed	Simulated dataset	1800	120
		1900	120
		2000	120
	Measured dataset	1800	120
		1900	10
		2000	120

Under the constant-speed condition, the simulated and measured vibration datasets both had 120 samples obtained at a speed of 1900 rpm. The bearing health statuses included a normal bearing and a defected bearing with an outer-race fault. The simulated and measured samples were preprocessed in the frequency domain to highlight the primary vibration characteristics. A total of 96 samples accounting for 80% of all samples were randomly used for training, and the remaining 20% were used for testing. The proposed hybrid modeling method consisted of a trained vibration generation network and a mapping network to be trained. The proposed hybrid model and the WGAN network were both trained 500 epochs. Figures 15 and 16 present vibration signals with an outer-race bearing fault at 1900 rpm, which were, respectively, obtained using the proposed hybrid model and the WGAN network. As can be observed from Figures 15b and 16b, the fault's characteristic frequency and its multiples of the frequency occur in the measured spectrum, whose amplitudes are prominent. The Pearson correlation was adopted to evaluate the consistency between the output signal of the hybrid method and the measured vibration signal. The Pearson coefficient between the two vibration spectra in Figure 15b is 0.89, indicating that the vibration signal output by the proposed hybrid model is strongly correlated with the measured signal. And, the Pearson coefficient between the two spectra in Figure 16b is 0.86, which also indicates that the signal output by the WGAN network is highly corrected with the measured signal. The above results prove that the proposed hybrid model and the WGAN network can effectively simulate the dynamic vibration response under the constant-speed condition when the number of vibration samples is relatively sufficient.

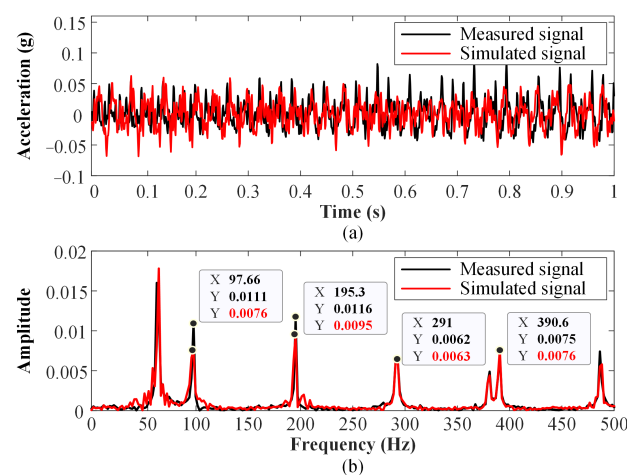


**Figure 15.** Comparison of the simulated vibration signal obtained using proposed hybrid modeling method and the signal measured under the constant-speed condition. (a) Vibration acceleration response, (b) frequency spectrum.

Under the variable-speed condition, the simulated dataset had a total of 360 samples obtained via numerical simulation at 1800 rpm, 1900 rpm, and 2000 rpm. The measured

dataset consisted of 240 samples collected using a sensor at 1800 rpm and 2000 rpm, with 10 samples at 1900 rpm. This is assumed to be a scenario with insufficient samples at 1900 rpm in actual applications. Figures 17 and 18 show the vibration signals with an outer-race bearing fault at 1900 rpm, which were, respectively, output by the proposed hybrid modeling method and the WGAN network. As can be seen in Figure 17a, the signal output by the proposed hybrid model approximates the measured vibration signal, and the MSE between the two signals is 0.0015. However, the MSE between the signal output by the WGAN network and the measured vibration signal in Figure 18a is 0.2658, which indicates that there exists a large difference between the two signals. Moreover, from the spectral perspective, the Pearson coefficient between the signal output by the proposed hybrid modeling method and the measured vibration signal in Figure 17b was calculated as 0.95, which represents a strong correlation. And, the Pearson coefficient between the signal output by the WGAN network and the measured signal was calculated as only 0.42. The weak correlation between the two signals shows that the WGAN network cannot perform accurate dynamic vibration modeling when the number of samples is insufficient in situations with different speeds. As a comparison, the data-driven characteristic of the WGAN network means that it needs to learn from a large amount of training data and then generate samples. As shown in Figure 16, when the number of samples at a constant speed are sufficient, the trained WGAN model can output vibration sequences with high accuracy. However, when the number samples for a certain speed are not sufficient, the model that is solely data-driven struggles to capture the complex relationship between the vibration characteristics of a rotor–bearing system and varying rotating speeds. This leads to large amplitude differences between the measured and simulated signals, especially for the amplitudes of each frequency component, as shown in Figure 18. In our proposed hybrid modeling method, the amount of simulated data at different rotational speeds provides the basic vibration characteristics. The effective combination of a large amount of simulated data and accurate measured data makes the hybrid modeling method able to output vibration responses with high accuracy. In conclusion, the above results demonstrate the effectiveness and superiority of proposed modeling method for simulating dynamic vibration responses, especially in scenarios with insufficient samples.

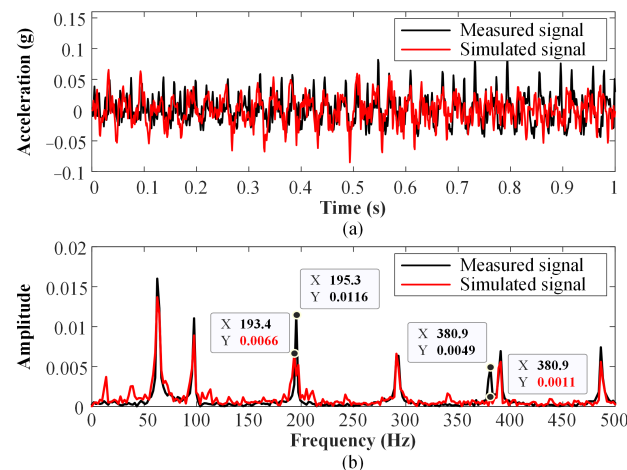


**Figure 16.** Comparison of the simulated vibration signal obtained using a WGAN network and the measured signal under the constant-speed condition. (a) Vibration acceleration response, (b) frequency spectrum.

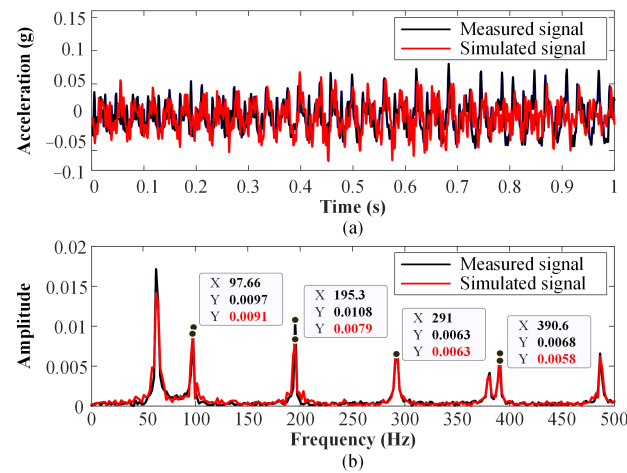


**Figure 17.** Comparison of the simulated vibration signal obtained using the proposed hybrid modeling and the measured signal under a variable-speed condition. (a) Vibration acceleration response, (b) frequency spectrum.

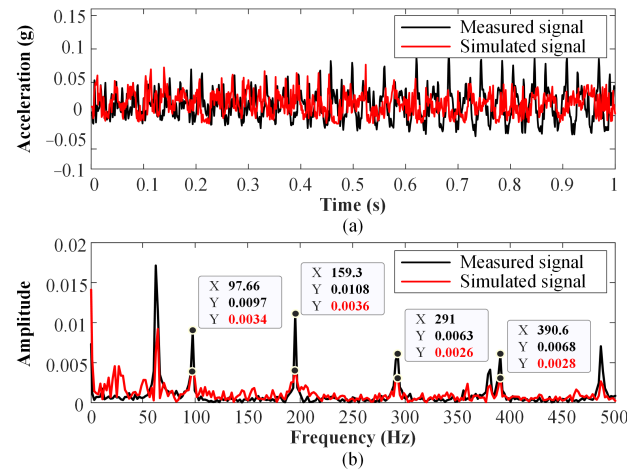


**Figure 18.** Comparison of the simulated vibration signal obtained by WGAN network and the measured signal under the variable-speed condition. (a) Vibration acceleration response, (b) frequency spectrum.

## 5. Conclusions

This study explored a physics-informed hybrid approach for modeling the dynamic vibrations of rotor–bearing systems, which integrates physics-based and data-driven modeling methods. A numerical simulation of a physics-based dynamic vibration model was firstly built using computer-aided technologies. Then, simulated vibration data obtained from numerical simulation, measured vibration data, and algorithms from the vibration generation network and data mapping network were combined to construct a physics-informed hybrid model. Finally, simulation and experimental results not only verified the feasibility of the physics-based model but also proved the effectiveness of physics-informed hybrid modeling for simulating dynamic vibration responses. Moreover, compared with a traditional data-driven modeling method, the simulated vibration signal output by the proposed hybrid modeling method is more consistent with the measured signals under both constant-speed and variable-speed conditions. For increasingly high-speed, complex, and automated rotating machinery, more complex operating conditions and composite fault types need to be considered in future work to establish a high-fidelity dynamics model.

**Author Contributions:** Conceptualization, M.Z. and C.P.; methodology, M.Z. and C.P.; software, B.Y. and Y.W.; validation, M.Z. and B.Y.; formal analysis, M.Z.; investigation, M.Z.; resources, C.P.; data curation, M.Z. and B.Y.; writing—original draft preparation, M.Z.; writing—review and editing, C.P. and B.Y.; visualization, M.Z. and Y.W.; supervision, C.P.; project administration, C.P.; funding acquisition, C.P. All authors have read and agreed to the published version of the manuscript.

**Funding:** This research was funded in part by the National Natural Science Foundation of China grant number 62122038 and in part by the Natural Science Foundation of Jiangsu Province grant number BK20211565.

**Data Availability Statement:** Data available on request from the authors.

**Conflicts of Interest:** The authors declare no conflict of interest.

## Nomenclature

$m_1, m_4$	equivalent masses of rotor at $O_1$ and $O_4$
$m_2, m_3$	masses of discs
$c_{s1}, c_{s2}$	damping of rotor at $O_1$ and $O_4$
$c_{d1}, c_{d2}$	damping of rotor at $O_2$ and $O_3$
$k_1, k_2, k_3, k_4$	stiffness of rotor at $O_1, O_2, O_3$ and $O_4$
$g$	acceleration due to gravity
$F_{bx}, F_{by}$	supporting forces of bearing in radial $x$ and $y$ directions
$k_b$	Hertz elastic coefficient
$j$	index of rolling elements
$N_b$	number of rolling elements
$\theta_j$	rotating angular at time $t$ of the $j$ th rolling element
$\delta_j$	contact deformation of the $j$ th rolling element
$\mu$	initial radial clearance of rolling bearing
$x_{in}, y_{in}$	displacements of the inner race in radial $x$ and $y$ directions
$x_{out}, y_{out}$	displacements of the outer race in radial $x$ and $y$ directions
$\beta$	switching variable indicating the health status of the bearing
$\delta_d$	displacement excitation caused by outer-race bearing fault
$\phi_0$	initial angular of defect area
$\phi_d$	span angular of defect area
$\delta_{dmax}$	maximum value of the displacement excitation
$r$	radius of rolling element
$L$	length of defect area
$k_{eq}$	stiffness coefficient of rolling bearing
$c_{eq}$	damping coefficient of rolling bearing
$F_{preload}$	preload of spring
$u_0$	displacement caused by preload
$F_j$	normal contact force
$d$	penetration depth
$\zeta$	force exponent
$K$	equivalent contact stiffness
$C$	equivalent contact damping
$x_j$	distance from geometry center of the $j$ th rolling element to raceway
$v_s$	slip velocity
$\mu_0$	coefficient of friction
$\mu_s$	static coefficient of friction
$\mu_d$	dynamic coefficient of friction
$V_s$	static transition velocity
$V_d$	dynamic transition velocity
$\omega$	rotor angular speed
$W$	width of defect area
$\lambda_1, \lambda_2$	optional weight coefficients
$T$	discrete Fourier transform

$\omega_{cage}$	rotating speed of cage
$\omega_{roller}$	rotating speed of rolling element
$r_c$	center-circle radius of rolling element
$\gamma$	ratio of rolling element radius $r$ to its center-circle radius $r_c$
$\omega_0$	rotating speed of bearing outer race
$f_{outer}$	fault characteristic frequency of outer-race fault

## References

- Zhu, W.; Lin, H.; Sun, W.; Wei, J. Vibration performance of traction gearbox of a high-speed train: Theoretical analysis and experiments. *Actuators* **2023**, *12*, 103. [\[CrossRef\]](#)
- Jafarian, M.; Nazarzadeh, J. Spectral analysis for diagnosis of bearing defects in induction machine drives. *IET Electr. Power Appl.* **2019**, *13*, 340–348. [\[CrossRef\]](#)
- Zhao, D.; Li, J.; Cheng, W.; Wen, W. Bearing multi-fault diagnosis with iterative generalized demodulation guided by enhanced rotational frequency matching under time-varying speed conditions. *ISA Trans.* **2023**, *133*, 518–528. [\[CrossRef\]](#) [\[PubMed\]](#)
- Zhu, D.; Gao, Q.; Sun, D.; Lu, Y. A detection method for bearing faults using complex-valued null space pursuit and 1.5-dimensional teager energy spectrum. *IEEE Sens. J.* **2020**, *20*, 8445–8454. [\[CrossRef\]](#)
- Rezamand, M.; Kordestani, M.; Orchard, M.E.; Cariveau, R.; Ting, D.S.K.; Saif, M. Improved remaining useful life estimation of wind turbine drivetrain bearings under varying operating conditions. *IEEE Trans. Ind. Inform.* **2020**, *17*, 1742–1752. [\[CrossRef\]](#)
- Wrzochal, M.; Adamczak, S. The problems of mathematical modelling of rolling bearing vibrations. *Bull. Pol. Acad. Sci.-Tech. Sci.* **2020**, *68*, 1363–1372.
- Singh, S.; Howard, C.; Hansen, C. An extensive review of vibration modelling of rolling element bearings with localised and extended defects. *J. Sound Vibr.* **2015**, *357*, 300–330. [\[CrossRef\]](#)
- McFadden, P.; Smith, J. Model for the vibration produced by a single point defect in a rolling element bearing. *Bull. Pol. Acad. Sci.-Tech. Sci.* **1984**, *96*, 69–82. [\[CrossRef\]](#)
- Su, Y.; Lin, S. On initial fault detection of a tapered roller bearing: Frequency domain analysis. *J. Sound Vibr.* **1992**, *155*, 75–84. [\[CrossRef\]](#)
- Liu, J. A dynamic modelling method of a rotor-roller bearing-housing system with a localized fault including the additional excitation zone. *J. Sound Vibr.* **2020**, *469*, 115144. [\[CrossRef\]](#)
- Wang, N.; Liu, M.; Yao, J.; Ge, P.; Wu, H. Numerical study on unbalance response of dual-rotor system based on nonlinear bearing characteristics of active magnetic bearings. *Actuators* **2023**, *12*, 86. [\[CrossRef\]](#)
- Li, Y.; Cao, H.; Niu, L.; Jin, X. A general method for the dynamic modeling of ball bearing-rotor systems. *J. Manuf. Sci. Eng.-Trans. ASME* **2015**, *137*, 021016. [\[CrossRef\]](#)
- Brouwer, M.; Sadeghi, F.; Ashtekar, A.; Archer, J.; Lancaster, C. Combined explicit finite and discrete element methods for rotor bearing dynamic modeling. *Tribol. Trans.* **2015**, *58*, 300–315. [\[CrossRef\]](#)
- Mishra, C.; Samantaray, A.K.; Chakraborty, G. Ball bearing defect models: A study of simulated and experimental fault signatures. *J. Sound Vibr.* **2017**, *400*, 86–112. [\[CrossRef\]](#)
- Liu, J.; Ni, H.; Li, X.; Xing, Q.; Pan, G. A simulation analysis of ball bearing lubrication characteristics considering the cage clearance. *J. Tribol.* **2023**, *145*, 044301. [\[CrossRef\]](#)
- Yu, Y.; Gao, H.; Zhou, S.; Pan, Y.; Zhang, K.; Liu, P.; Yang, H.; Zhao, Z.; Madyira, D.M. Rotor faults diagnosis in PMSMs based on branch current analysis and machine learning. *Actuators* **2023**, *12*, 145. [\[CrossRef\]](#)
- Popescu, T.; Aiordachioaie, D. Fault detection of rolling element bearings using optimal segmentation of vibrating signals. *Mech. Syst. Signal Proc.* **2019**, *116*, 370–391. [\[CrossRef\]](#)
- Yan, T.; Wang, D.; Xia, T.; Xi, L. A generic framework for degradation modeling based on fusion of spectrum amplitudes. *IEEE Trans. Autom. Sci. Eng.* **2020**, *19*, 308–319. [\[CrossRef\]](#)
- Wang, Y.; Yang, M.; Li, Y.; Xu, Z.; Wang, J.; Fang, X. A multi-input and multi-task convolutional neural network for fault diagnosis based on bearing vibration signal. *IEEE Sens. J.* **2021**, *21*, 10946–10956. [\[CrossRef\]](#)
- Wang, H.; Li, C.; Du, W. Coupled hidden Markov fusion of multichannel fast spectral coherence features for intelligent fault diagnosis of rolling element bearings. *IEEE Trans. Instrum. Meas.* **2021**, *70*, 1–10. [\[CrossRef\]](#)
- Shao, S.; Wang, P.; Yan, R. Generative adversarial networks for data augmentation in machine fault diagnosis. *Comput. Ind.* **2019**, *106*, 85–93. [\[CrossRef\]](#)
- Zhou, Q.; Hu, Y.; Liu, J. A novel assessable data augmentation method for mechanical fault diagnosis under noisy labels. *Measurement* **2022**, *198*, 111114.
- Liu, S.; Jiang, H.; Wu, Z.; Li, X. Data synthesis using deep feature enhanced generative adversarial networks for rolling bearing imbalanced fault diagnosis. *Mech. Syst. Signal Proc.* **2022**, *163*, 108139. [\[CrossRef\]](#)
- Jeong, H.; Bai, J.; Batuwatta-Gamage C.P.; Rathnayaka, C.; Zhou, Y.; Gu, Y. A physics-informed neural network-based topology optimization (PINNTO) framework for structural Optimization. *Eng. Struct.* **2023**, *278*, 115484. [\[CrossRef\]](#)
- Chaiprabha, K.; Chanchaoren, R. A deep trajectory controller for a mechanical linear stage using digital twin concept. *Actuators* **2023**, *12*, 91. [\[CrossRef\]](#)

26. Li, L.; Li, Y.; Du, Q.; Liu, T.; Xie, Y. ReF-nets: Physics-informed neural network for Reynolds equation of gas bearing. *Comput. Meth. Appl. Mech. Eng.* **2022**, *391*, 115484. [[CrossRef](#)]
27. Thelen, A.; Zhang, X.; Fink, O.; Lu, Y.; Ghosh, S.; Youn, B.D.; Todd, M.D.; Mahadevan, S.; Hu, C.; Hu, Z. A comprehensive review of digital twin—Part 1: Modeling and twinning enabling technologies. *Struct. Multidiscip. Optim.* **2022**, *65*, 354. [[CrossRef](#)]
28. Lai, X.; Wang, S.; Guo, Z.; Zhang, C.; Sun, W.; Song, X. Designing a shape-performance integrated digital twin based on multiple models and dynamic data: A boom crane example. *J. Mech. Des.* **2021**, *143*, 071703. [[CrossRef](#)]
29. Piltan, F.; Kim, J. Crack size identification for bearings using an adaptive digital twinn. *Sensors* **2021**, *21*, 5009. [[CrossRef](#)]
30. Qin, Y.; Wu, X.; Luo, J. Data-model combined driven digital twin of life-cycle rolling bearing. *IEEE Trans. Ind. Inform.* **2021**, *18*, 1530–1540. [[CrossRef](#)]
31. Wang, J.; Ye, L.; Gao, R.X.; Li, C.; Zhang, L. Digital Twin for rotating machinery fault diagnosis in smart manufacturing. *Int. J. Prod. Res.* **2019**, *57*, 3920–3934. [[CrossRef](#)]
32. *MSC ADAMS Reference Manual*; MSC Software Corp.: Newport Beach, CA, USA, 2012. Available online: <https://www.mscsoftware.com/product/adams> (accessed on 21 February 2017).
33. Giesbers, J. Contact Mechanics in MSC Adams—A Technical Evaluation of the Contact Models in Multibody Dynamics Software MSC Adams. Bachelor's Thesis, University of Twente, Enschede, The Netherlands, 2012.
34. Tu, W.; Liang, J.; Yu, W.; Shi, Z.; Liu, C. Motion stability analysis of cage of rolling bearing under the variable-speed condition. *Nonlinear Dyn.* **2023**, *111*, 11045–11063. [[CrossRef](#)]

**Disclaimer/Publisher's Note:** The statements, opinions and data contained in all publications are solely those of the individual author(s) and contributor(s) and not of MDPI and/or the editor(s). MDPI and/or the editor(s) disclaim responsibility for any injury to people or property resulting from any ideas, methods, instructions or products referred to in the content.